

Research article

3D morphometry of endothelial cells angiogenesis in an extracellular matrix composite hydrogel

Faranak Heidari^{a,b}, Parisa Shamshiripour^{c,d}, Mehrana Rahnama^e,
Maryam Saadatmand^a, Davoud Ahmadvand^d, Sara Simorgh^{f,g,*},
Ali-Reza Moradi^{h,i,**}

^a Department of Chemical and Petroleum Engineering, Sharif University of Technology, Tehran, Iran

^b Division of Pharmacology, Utrecht Institute for Pharmaceutical Sciences, Utrecht University, Utrecht, the Netherlands

^c Department of Medicine, Iran University of Medical Sciences (IUMS), Tehran, Iran

^d Department of Molecular Imaging, Faculty of Advanced Technologies in Medicine, Iran University of Medical Sciences (IUMS), Tehran, Iran

^e Department of Biotechnology, Faculty of Biological Sciences, Alzahra University, Tehran, Iran

^f Cellular and Molecular Research Center, Iran University of Medical Sciences, Tehran, Iran

^g Department of Tissue Engineering and Regenerative Medicine, Faculty of Advanced Technologies in Medicine, Iran University of Medical Sciences, Tehran, 1591639675, Iran

^h Department of Physics, Institute for Advanced Studies in Basic Sciences (IASBS), Zanjan, 45137-66731, Iran

ⁱ School of Nano Science, Institute for Research in Fundamental Sciences (IPM), Tehran, 19395-5531, Iran

A B S T R A C T

Human umbilical vein endothelial cells (HUVECs) play a fundamental role in angiogenesis. Herein, we introduce digital holographic microscopy (DHM) for the 3D quantitative morphological analysis of HUVECs in extracellular matrix (ECM)-based biomaterials as an angiogenesis model. The combination of volumetric information from DHM and the physicochemical and cytobiocompatibility data provided by fluorescence microscopy and cytology offers a comprehensive understanding of the angiogenesis-related parameters of HUVECs within the ECM. DHM enables label-free, non-contact, and non-invasive 3D monitoring of living samples in real time, in a quantitative manner. In this study, the human amniotic membrane (HAM) is decellularized, pulverized, and combined with sodium alginate hydrogel to provide an *in vitro* substrate for modeling HUVEC angiogenesis. Our results demonstrate that modifying alginate hydrogel with HAM enhances its biofunctionality due to the presence of ECM components. Moreover, the DHM results reveal an increase in its porous properties, which, in turn, aids in interpreting the tubulation results.

1. Introduction

Angiogenesis, the sprouting of new blood vessels from pre-existing ones, occurs in various pathological and physiological conditions. It plays a crucial role in tissue regeneration, particularly in wound healing, retinopathies, and tumor growth [1–5]. Endothelial cells play a key role in this process. In response to stimuli, such as acute tissue injury, these cells begin sprouting from the original vessel, proliferate, migrate, and align to form a lumen, and eventually generating new blood vessels [6,7]. A comprehensive understanding of this process is indispensable for the assessment of this phenomenon for both pharmacological applications and therapeutic approaches [8]. Additionally, other fields of interest, such as stem cell research, need live monitoring of proliferation, differentiation, and angiogenic capacities of endothelial progenitor cells [9]. Accordingly, to assess angiogenic characteristics and evaluate various

* Corresponding author at: Cellular and Molecular Research Center, Iran University of Medical Sciences, Tehran, Iran.

** Corresponding author at: Department of Physics, Institute for Advanced Studies in Basic Sciences (IASBS), Zanjan, 45137-66731, Iran.

E-mail addresses: sara.simorgh@iums.ac.ir (S. Simorgh), moradika@iasbs.ac.ir (A.-R. Moradi).

<https://doi.org/10.1016/j.heliyon.2024.e39616>

Received 8 July 2024; Received in revised form 30 September 2024; Accepted 18 October 2024

Available online 21 October 2024

2405-8440/© 2024 The Author(s). Published by Elsevier Ltd. This is an open access article under the CC BY-NC-ND license (<http://creativecommons.org/licenses/by-nc-nd/4.0/>).

angiogenic cytokines, such as vascular endothelial growth factor (VEGF) and transforming growth factor β (TGF- β), etc., numerous *in vitro* and *in vivo* experimental models have been established [2].

In the body, basement membranes, which are soft and extremely specialized extracellular matrix (ECM), enclose the human umbilical vein endothelial cells (HUVECs) [10,11]. ECM scaffolds regulate cell interaction, migration, differentiation, and proliferation [12–17]. Seeding HUVECs over a basement membrane instigates them to form vascular-like structures to imitate angiogenesis *in vitro* [18–20]. The composition and presence of the basement membrane layer significantly influences the effectiveness of tube formation. Various types of basement membranes, such as collagen, Matrigel, and other hydrogel matrices, can be used. Incorporating cell motifs, like arginine-glycine-asparagine (RGD) protein ligands, can modify the biomaterial's surface, enhancing both cell function and cell-matrix interactions [11].

In this study, we mimic the native ECM for HUVECs by synthesizing a composite hydrogel composed of alginate and decellularized human amniotic membrane (HAM) as an RGD-containing basement membrane. While alginate is one of the most widely used biomaterials in tissue engineering, it lacks essential cell motifs [5,21–23]. To overcome this drawback of alginate, we blend it with powdered HAM. The HAM is a thin inner layer of the embryonic membrane that surrounds the fetus and encompasses a variety of components, such as various types of collagen, fibronectins, and laminin [24–27]. Considering its superb physiological characteristics, it is widely used in skin dressing and as a graft for corneal treatment [28]. Furthermore, solubilizing the ECM can either impair some of its components and reduce bioactivity or introduce potential cytotoxicity due to the use of organic solvents [5,29–32]. Instead, we utilize powdered HAM, which has previously been employed to introduce cardiac patches through homogenization into a secondary hydrogel [33,34]. Mounting the previous evidence, numerous attempts have been devoted to enhance the resemblance of *in vitro* HUVEC tubulation assays to the actual processes occurring in the body, as well as to introduce novel analytical methods for better interpretation of the results [35–39]. A primary concern for such studies, however, is the imaging procedure with bright-field or fluorescent microscopy, as 2D imaging modalities. On the other hand, the heterogeneity of angiogenesis requires 3D microvascular data for more reliable quantification; otherwise, important features of the process may be overlooked. Since HUVEC tubulation is a 3D process, the absence of detailed analytical methods to capture 3D images limits the advantages of *in vitro* tubulation analysis [40]. To provide more accurate information on morphological features and improve characterization, quantitative 3D high-definition imaging should be performed. Additionally, the use of fluorophore probes for fluorescence microscopy poses a significant drawback, as it requires sample fixation and may introduce unwanted background interference [41] and a probe/label free approach is required. Other imaging modalities, such as confocal microscopy, which inherently involve scanning, are useful for many microscopic specimens but are limited to fixed samples.

In this paper, we introduce digital holographic microscopy (DHM) in transmission mode as an elegant methodology to overcome the aforementioned shortcomings of bright-field, fluorescent, and confocal microscopies: DHM is label-free, unlike fluorescent microscopy, quantitative, unlike DIC and Zernike phase contrast microscopy, and single exposure, unlike confocal microscopy [42–44]. These features fit very well for a large class of important samples, such as living matter. It has been utilized for various biological studies over the last two decades [44–51]. We apply DHM for a quantitative investigation of endothelial cell angiogenesis. To obtain comprehensive information about the samples, we also acquire fluorescent microscopy images and use several other characterization techniques. Additionally, we use the Angiogenesis Analyzer plugin in ImageJ to evaluate tube formation. The 3D DHM data then provide additional morphometric information on the tubulated HUVECs.

In Section 2, sample preparation, initial characterization information, experimental setup, and numerical DHM processing procedure are presented. In Section 3 the experimental results are shown and discussed. The paper is concluded in Section 4.

2. Methods and materials

2.1. Materials

Dulbecco's modified Eagle's medium F-12 (DMEM-F12), Pen-Strep and fetal bovine serum (FBS) are bought from Bioidea (Tehran, Iran). Ethylene diamine tetra acetic acid (EDTA), $MgCl_2$, HCl, chloroform, phenol, Tris-hydrochloric acid (Tris-HCl), Tris, sodium dodecyl sulfate (SDS), Bovine Serum Albumin (BSA), and isoamyl alcohol buffer are purchased from Merck KGaA Germany. Hematoxylin and eosin (H&E), and Masson's trichrome (MT) are bought from Merck, Germany. Sodium Alginate (Na-Alg, medium viscosity 180947-100G) is purchased from Sigma-Aldrich, Germany. The human umbilical vein endothelial cells (HUVECs) line is bought from the National cell bank, Pasteur Institute, Iran. The live/dead cytotoxicity kit is purchased from Kiazist (Tehran, Iran). Similarly, lysis buffer is produced from AZMAELIXIR, Iran.

2.2. Decellularization process

We decellularize HAM using Enzyme-based decellularization protocol, which is among the most viable and safe methods developed for decellularization of HAM [5,52,53]. The HAM is acquired from Ghiassi Hospital (Tehran, Iran) from mothers who gave birth under cesarean conditions. All mothers are checked in terms of not having syphilis, hepatitis B and C, and human immunodeficiency virus (HIV). Firstly, the additional tissues are separated and the membranes are washed completely, exerting Phosphate Buffered Saline (PBS) solution consisting of 1 mL/L Pen-Strep and 100 mL/L Aprotinin (PBS-1x, pH=7.4) to eliminate all blood clots. Afterward, we manually sequester the chorionic membrane of HAMS and rewash it using PBS. Then, the HAMS are sliced into almost 2 mm² pieces, and are soaked in a solution encompassing 1 g.L⁻¹ of EDTA and 1.2114 g.L⁻¹ Tris (pH=7.6, for 16 hours, at 4 °C). Similarly, the sectioned HAMS are placed into a solution encompassing 1 g.L⁻¹ EDTA, 0.3 g.L⁻¹ SDS, 1 mL.L⁻¹ Pen-Strep, and 100 μ L.L⁻¹ Aprotinin

and after 5 hours of shaking at 100 rpm and room temperature, this solution is renewed, and shaking is continued for 24 hours. Thereafter, the samples are washed by applying PBS, and again a solution (pH=7.5) comprising 50 mg.L⁻¹ BSA, 6.88 g.L⁻¹ Tris-HCl, and 0.95211 g.L⁻¹ MgCl₂ is added, and the samples are shaken in a shaker-incubator for 4 hours (100 rpm, 37 °C). After completing the decellularization, the samples are washed three times to remove cell debris by taking advantage of another solution (pH=7.6) containing 6.057 g.L⁻¹ Tris and 8.766 g.L⁻¹ HCl. Eventually, the decellularized tissues are put in a freezer at -80 °C for 24 hours, and then they are lyophilized and powdered using a mixer miller (NARYA-BM25, Amin Asia, Iran). Written informed assent is acquired from all donors who consented to donate samples for this study. The harvest and decellularization protocols are approved by the Research Ethics Committee of Iran University Medical of Sciences, Tehran, Iran (Ethical code: IR.IUMS.REC.1400.984).

2.3. Histological analysis

To determine the advantages of the decellularization protocol, histological analyses are fulfilled [52]. Fresh HAM and decellularized HAM are placed into a 10% PBS/neutral buffered formalin. The samples are washed utilizing distilled water and dehydrated by applying graded alcohol series. Afterward, they are placed in paraffin and chopped into nearly 5 μm pieces. Finally, hematoxylin and eosin (H&E), and Masson's trichrome (MT) are exerted to stain the tissues, and an inverted microscope (ZEISS, Carl Zeiss NTS Ltd, Germany) and follow-up histological analysis is used to characterize decellularization.

2.4. Size distribution report of powdered HAM

The size distribution of the aqueous solution of powdered HAM is carried out using dynamic light scattering (DLS) measurements [54]. Calculations are performed at 25 °C, and the results are reported in terms of intensity.

2.5. Preparing hydrogels and characterization

Evidently, considering the physiochemical characteristics of the matrix provides insight into cell-cell and cell-matrix interactions. In our previous study, we elaborated on the mechanical characteristics of the hydrogel and their influence on the matrix biocompatibility [5]. We incorporated several ratios of decellularized HAM (0%, 0.4%, 0.6%, and 0.8% w/v) inside 4% (w/v) of alginate. Various concentrations of the hydrogel were evaluated from disparate points of view like biocompatibility, mechanical characteristics, porosity, and degradation ratio. Overall, according to the acquired results, biocompatibility and cell proliferation of the hydrogel were boosted significantly by incorporating more decellularized HAM owing to the augmentation of cell motifs, laminin, and various types of collagen, which brings about an increase in cell attachment, migration, cell-cell and cell matrix interactions. However, the matrix with 0.8% decellularized HAM demonstrated less proliferation compare with 0.6%. The reduction of porosity by increasing the ratio of decellularized HAM, and subsequently declining of the migration and ECM secretion ambient is one of the subjects that may account for this reduction. Similarly, this ratio demonstrated an elastic modulus of 32.35 ± 5 kPa, which seems to be proper for tissue engineering applications as the Young's modulus reported for myocardial tissues is 20-51 kPa for rat, 12-198 kPa for porcine, 19-192 kPa for ovine, and <50 kPa for a healthy human heart, which can increase to >100 kPa under pathological situations [5].

Alginate-based hydrogels have always been a favorable environment in tissue engineering and regenerative medicine due to their tunable mechanical and degradative properties. The mechanical characteristics of the engineered hydrogel should replicate the native tissue stiffness, elasticity, and viscoelasticity to provide favorable environment for cell proliferation, migration, and differentiation. Furthermore, key factors for tissue formation and function like spreading, polarizing, and aligning of cells are directly affected by mechanical properties of the hydrogels. Varying factors like crosslinking density, alginate concentration, and the molecular weight of the alginate can adjust the mechanical properties of alginatebased hydrogels. Higher alginate concentrations generally lead to stiffer hydrogels, which can be used to guide cell behavior according to the mechanical cues required. Moreover, by adjusting the concentration of crosslinking agents, such as calcium ions in ionically crosslinked alginate, the stiffness and the mechanical resilience of the hydrogel can be precisely controlled. In addition, mixing alginate with other biopolymers like collagen allows the creation of hydrogels with a wide range of mechanical properties, which can be tailored to specific tissue engineering applications. Numerous studies assessed these factors [55–57]. We, however, just tune our hydrogel mechanical elasticity by mixing alginate with various ratios of decellularized HAM. One of the other key factors that should be taken into account is the hydrogel degradability. The degradative properties of the hydrogel can modulate cell behavior. As the hydrogel degrades, it releases the cells and bioactive factors in a controlled manner, providing space for tissue growth and allowing cells to remodel the surrounding matrix. This promotes tissue maturation and integration. Alginate-based hydrogels are generally non-degradable in physiological conditions, but their degradation can be controlled by modifications or by blending with degradable polymers. In our previous study, we illustrated that the degradation rate is declined by the addition of decellularized HAM from $69.3 \pm 3.64\%$ for alginate hydrogel to $51.8 \pm 3.8\%$ for the modified alginate with 0.6% of decellularized HAM, and $44.9 \pm 4.1\%$ for the alginate with the 0.8% decellularized HAM. While we expected that higher ratio of decellularized HAM would display more proliferation owing to the higher ratio of RGD protein motifs, the composite with 0.8% of decellularized HAM demonstrated less proliferation compared with the composite with 0.6% of decellularized HAM. The reduction of degradability might account for this behavior, since cells didn't have enough space for growth, migration, and secretion of ECM. Hence, adjusting the concentration of the prepared hydrogel would control degradation, allowing cells to interact more directly with the matrix, promoting adhesion, migration, and growth.

In this study, we select 0.6% of decellularized HAM for further investigations, as we believe that it not only contains natural ECM for enhancing cell proliferation and appropriate cytokines for inducing angiogenesis, but also this ratio seems to be adequate for

providing sufficient space for cell migration, proliferation, newly secreted ECM, and neovascularization, while its elastic modulus is in the tailored range for regenerative medicine applications. First, two groups of alginate hydrogels are prepared according to the previous protocols [58]; preferably, 4% (w/v) alginate powder is dissolved in DMEM-F12 including 1% Pen-Strep, for 3-4 hours under continuous stirring in sterile conditions, then modified alginate, which encompasses 4% (w/v) alginate powder and 0.6% (w/v) HAM powder is dissolved in DMEM-F12, including 1% Pen-Strep, for 3-4 hours under continuous stirring. The prepared hydrogels are transmitted to culture plates, and 100 μL of CaCl_2 (4% w/v) is added to each well. After a minute, when the hydrogels are crosslinked, the CaCl_2 is removed and 0.5×10^6 cells/mL HUVECs are seeded on each group. Then, 150 μL of complete cell culture media (DMEM-F12, 10% FBS, and 1% Pen-Strep) is added to each well. The culture plate is incubated at 37 °C, 5% CO₂, and 95% relative humidity, and the medium is renewed. In this research four groups are designed as follows:

- i. Alginate hydrogel (4% w/v alginate without cell)
- ii. Modified alginate hydrogel (4% w/v alginate+ 0.6% w/v dHAM without cell)
- iii. Alginate hydrogel + HUVECs (Group A)
- iv. Modified alginate hydrogel + HUVECs (Group B)

2.6. Fourier transform infrared (FTIR) spectroscopy

FTIR is performed for alginate and modified alginate hydrogel groups [59]. The freeze-dried hydrogels are pulverized and mixed with potassium bromide. These compounds are pressed in tablet form and afterward fastened on a FTIR spectrometer (PerkinElmer Co., USA) to distinguish the chemical functional groups. The average of 128 scans, each at a resolution of 4 cm^{-1} and at a temperature of 25 °C, are used to generate the spectra.

2.7. Biocompatibility assay

To recognize the cell viability of the experimental groups, an MTT and live/dead kit are employed to assess cell viability and measure cell proliferation according to the manufacturer's protocol [60]. Briefly, on days 1, 3, and 7, the medium within cultured plates is renewed with fresh DMEM-F12 containing a 10 μL MTT kit. The culture plate is placed in a light-isolated incubator (37 °C, 5% CO₂, and 95% relative humidity) for 4 hours. Then, the medium of each well is replaced by a 100 μL solubilized solution. Finally, the absorbance is measured at 570 nm using a microplate reader (Bio-Rad Laboratories, Hercules, CA). Similarly, a 2D cell culture medium is determined as a control group.

Furthermore, after 48 hours of incubation of the cell culture, 1 mL of cell culture medium encompassing the live-dead kit is added to each well and again placed into the light avoided condition at 37 °C, 5% CO₂, and 95% relative humidity for 15 minutes [61]. Then, PBS is used to wash each well, and the Olympus IX70 fluorescence microscope is utilized to observe and picture hydrogels. It should be noted that fluorescent diacetate (FDA) is diffused into the encapsulated hydrogels and stains living cells in green, and propidium iodide (PI) is diffused into the encapsulated hydrogels and dyes the dead cells in red. Four pictures of each well are taken by a camera (Orca Flash 4.0 LT Plus, Hamamatsu, 6.5 μm pixel pitch) connected to the fluorescence microscope.

2.8. Field emission scanning electron microscopy (FE-SEM)

The morphology of alginate and modified alginate is initially characterized using FE-SEM (TESCAN MIRA 3LMU, Czechia) with a 30 kV operating voltage to determine the presence of powdered HAM on the surface of the lyophilized hydrogels, and to measure the changes in the roughness of the surfaces, pore size, and pore distribution of the hydrogels. Briefly, the surface of the freeze-dried hydrogels is coated with a thin layer of gold and is settled on aluminum stubs. Images are captured using FE-SEM and the average pore size is reported by measuring the size of 10 random pores via ImageJ software [62].

2.9. 2D endothelial tube formation assay (ETFA)

ETFA is accomplished to determine the angiogenesis and tubulation of HUVECs by imaging and observing the encapsulated cells' morphology over time [1,5,6]. ETFA is performed by analyzing live/dead fluorescence images after 5 days, as an indicator to illustrate the morphology of HUVECs and their tubulation in each group, using ImageJ analyzer software's "Angiogenesis Analyzer" plugin. This assay is implemented by detecting formed tree structures via analyzing the vectorial objects (Nodes, Extremities, Junctions, Branches, Segments, and Meshes) defined in Table 1.




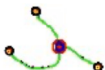
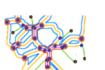
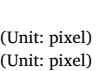
2.10. 3D analysis of hydrogel structures and tube formation

2.10.1. Digital holographic microscopy (DHM) setup

DHM provides useful data on the phase of the incident transmitted light which may be further visualized by 3D reconstruction. For most of the transparent samples, such as biological specimens, a Mach-Zehnder arrangement is the most common approach to set up the DHM setup. Fig. 1 depicts in detail the Mach-Zehnder arrangement that we use in the current study. The He-Ne laser (MEOS) which works at 632 nm, provides a highly coherent and stable beam and is used as the illumination source. The beam is collimated by lens CL after spatially filtering by the combination of a 4x microscope objective MO1 and a 20 μm pinhole PH, placed in the Fourier

Table 1

Vectorial objects.

Vectorial Objects	Definition	Form or Unit
Node	The smallest element (a pixel) of a skeletonized tree causes a bifurcation, and each of them is connected to three adjacent pixels (green pixels linked to red ones).	
Junction	A group of adjacent pixels makes a bifurcation (red pixels). Junctions are demonstrated as a red dot bordered by a blue circle.	
Extremity	Extremities are related to those of pixels connected to only one adjacent pixel (red pixels). Extremities are shown as red dots bordered by a yellow square and black circle.	
Branch	Branches are green lines connecting one junction and one extremity.	
Segment	Segments are magenta and yellow lines linking two junctions.	
Mesh	Associated to the closed area bounded via segments and related junctions (blue area).	
Mean Mesh Size	The average value of Mesh size on each picture.	(Unit: pixel)
Total Mesh Size	Sum of Mesh area on each picture.	(Unit: pixel)
Total Segment Length	The sum of Segment length per picture.	(Unit: pixel)
Total Branches Length	Sum of Branches length per picture.	(Unit: pixel)
Total Length	The sum of Segments and Branches length per picture.	(Unit: pixel)

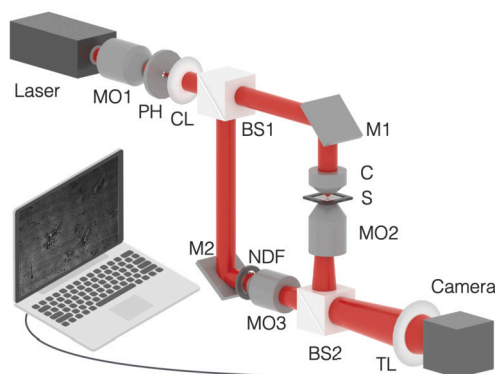


Fig. 1. DHM setup. Mach-Zehnder arrangement for holographic imaging of HUVEC Cells, Hydrogels, and tube formation assay. Laser: He-Ne, 632.8 nm, He-Ne; MO: microscope objective; PH: pinhole; CL: collimating lens; BS: beam splitter; M: mirror; C: condenser; S: sample; NDF: neutral density filter; TL: tube lens.

plane of MO1. The collimated beam is split into two beams: the object beam and the reference beam. The object beam is directed onto the sample under study (S) by the 45° mounted mirror M1. The condenser C condenses the laser beam onto the sample to provide a sufficient and uniform laser beam throughout the whole field of view. The scattered light carrying the information of the object is collected by the objective lens MO2 and is redirected by BS2 onto the tube lens TL and the digital camera (DCC1545M, Thorlabs, 8bit dynamic range, $5.2 \mu\text{m}$ pixel pitch). The reference beam is the reflected beam from BS1 and after reflection from M2 passes through a neutral density filter, NDF, and MO3 is combined with the object beam at BS2, and finally their interference forms the digital hologram on the camera. The NDF is used to match the intensity of the two interfering beams, and this is required to achieve high contrast interference fringes in the recorded holograms. The role of the additional objective lens MO3 is also crucial. It guarantees the wavefront curvature radius matching of the beams. This way, obtaining linear and uniform fringes with adjustable density of fringes will be possible. These are the requirements for suitable 3D image reconstruction from the recorded digital holograms. The digital holograms are recorded as a successive image file such as *.tiff files. Therefore, monitoring dynamic phenomena in 3D at the recording speed of the digital camera becomes possible. The optical elements in the DHM setup, the sample chamber and the entrance glass of the camera can always cause contaminations and optical aberrations. An important feature of DHM is that we can record a reference hologram when the sample is removed from the setup. Then, in the reconstruction stage the disturbing effects can be subtracted by having the phase and amplitude information of the reference hologram.

2.10.2. Numerical reconstruction procedure

The digital holograms of the samples that are recorded during the experiment are subjected to numerical reconstruction toward extracting volumetric information. These holograms are indeed the intensity distribution associated with the interference of the reference beam (E_r) and the object beam (E_o) at $z = 0$ plane:

$$I(x, y, 0) = |E_r(x, y)|^2 + |E_o(x, y)|^2 + E_r(x, y)E_o^*(x, y) + E_o^*(x, y)E_r(x, y). \quad (1)$$

The reconstruction procedure includes illumination of the hologram by the reference beam, followed by propagation into a demanded plane of reconstruction, z , and eventually extracting the phase and intensity distributions from the propagated complex field, which are done numerically by a computer on the stored image files. However, the important feature of digital holography is that further actions, such as applying the required smoothing and denoising filtering and removing the unwanted light beams that are caused by the first three terms of Eq. (1), can also be done during the reconstruction stage. This feature, unlike conventional holography, makes the technique suitable for the investigation of dynamic phenomena, such as the current research. The numerical reconstruction is actually the calculation of diffraction through the Fresnel-Kirchhoff integral. The most common approach to calculating the above integral, which is also pursued here, is the angular spectrum propagation (ASP) method. In ASP, the intensity distribution of Eq. (1) is first transformed into Fourier space, and adjustable filters to remove the unwanted terms and phase smoothing are applied. The filtered spectrum is propagated to the reconstruction plane z and its Fourier transform is taken, which will be the whole complex field of the reconstructed image. The whole procedure is also applied to the reference digital hologram (the recorded hologram when the specimen is removed), and its reconstructed phase and amplitude are subtracted from those of the main hologram. The reconstructed complex field after subtraction of the reference hologram provides the intensity distribution and the phase map as follows:

$$I_s(x, y, z) = |E_s^F(x, y, z)|^2, \quad (2)$$

$$\phi_s(x, y, z) = \tan^{-1} \frac{\text{Im}[E_s^F(x, y, z)]}{\text{Re}[E_s^F(x, y, z)]}, \quad (3)$$

where, $E_s^F(x, y, z)$ is the reconstructed complex field. $\phi_s(x, y, z)$ is related to the physical thickness and the refractive index at each point throughout the sample by

$$\phi_s(x, y) = \frac{2\pi}{\lambda} n(x, y) d(x, y). \quad (4)$$

For many specimens, the variations of the refractive index can be neglected, and therefore the thickness distribution, i.e., 3D images, of a transparent phase object, such as the cells of current research, may be extracted [44,63]. The resulting 3D maps can also be used for further quantitative investigations of the samples. Various morphometrical parameters can be obtained if the thickness at each point is known. The mean height, volume, standard deviation, skewness, kurtosis, longevity, circularity, etc. can be easily obtained. These parameters have been defined in our previously published study [63]. Amongst, we calculate volume, skewness, and kurtosis to assess the samples. The 3D quantitative information within arbitrary time scales and within the recording device's speed capability is a treasure for biological and other dynamic samples.

2.11. Statistical analysis

The acquired data are presented as mean values along with associated standard deviations. The averaging is performed on at least three experimental measurements. One-way analysis of variance (ANOVA) is used to analyze the statistical data. Data analysis is accomplished with GraphPad InStat software and a p-value of $p < 0.05$ is considered significant.

3. Results and discussion

3.1. Verification of decellularization

The simplest way for checking the decellularization effectiveness is to monitor the changing color from red (pertaining to myoglobin) to white, pertinent to the collagen content of the tissues [64]. Similarly, histological stains are favorable tissue dyes for decellularization assays [54]. H&E stain the cell's nucleus dark blue/purple and the ECM and cytoplasm pink. Figs. 2(a) and 2(b) are the images of fresh and decellularized HAM, respectively, after applying the H&E assay. The disappearing of dark blue regions in Fig. 2(b) shows that all cells' nuclei are wiped out and only the ECM is preserved, confirming the efficacy of the decellularization procedure. Figs. 2(c) and 2(d) are similar images after staining with MT dyes. MT dyes indicate the cell's nucleus dark red/brown and the collagen blue. The MT staining demonstrates that all cells are eliminated, and a significant amount of collagenous tissue is remained in the decellularized tissue. These findings suggest that both H&E and MT staining can be reliable methods to assess the effectiveness of decellularization procedures.

3.2. Size distribution report of powdered HAM

According to the report of size distribution analysis via DLS (Fig. 2(e)), the HAM particles possess an average efficient diameter of approximately 1712 nm with polydispersity index (PDI) of 0.352, and more than 45% intensity.

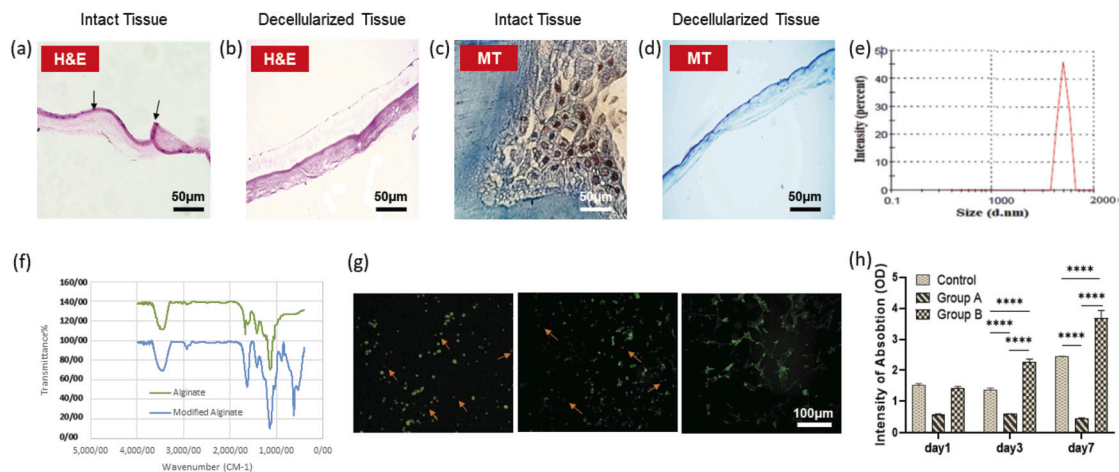


Fig. 2. H&E staining images of (a) fresh human amniotic membrane and (b) decellularized tissue. MT staining images of (c) fresh human amniotic membrane and (d) decellularized tissue. Black arrows show cell nuclei. (e) Size distribution analysis provided by DLS test. (f) FTIR of Alginate and Modified Alginate hydrogel groups. (g) live/dead staining of the control group (2D cell culture plate), Group A, and Group B illustrating cell viability after 48 hrs. Red dots are dead cells demonstrated by orange arrows. (h) MTT analysis of Group A and Group B demonstrates cell viability and proliferation of HUVECs. Significant difference is observed between Group A and Group B compared with each other and with the control group (**** $P < 0.0001$).

3.3. Characterization of hydrogel groups with FTIR

FTIR is carried out to evaluate the composition of the prepared hydrogels. FTIR is a commonly used technique for identifying functional groups in samples and is particularly useful for characterizing biomolecules such as proteins and carbohydrates [65]. As shown in Fig. 2(f), alginate hydrogel shows a peak at 3410.7 cm^{-1} and two other peaks at 1135 cm^{-1} and 1430.2 cm^{-1} which, respectively, are correlated to C-O stretching vibration and the symmetric COO-functional group. These results are consistent with the chemical structure of alginate, which is a linear polymer composed of repeating units of α -L-guluronic acid and β -D-mannuronic acid [66–68]. Likewise, the modified alginate hydrogel (alginate + HAM) demonstrates significant absorbance at 3453 cm^{-1} of N-H stretching (Amide A) and 2932 cm^{-1} of asymmetric CH₃ (Amide B), both of which are related to ECM protein of HAM. Also, symmetric CH₃ collagen (related to ECM protein of HAM) is illustrated at 1427 cm^{-1} , and C-O stretch is manifested at 1129 cm^{-1} which is consistent with the presence of carboxyl groups in the modified alginate [5,69,70].

3.4. Biocompatibility evaluation of hydrogel groups

Live/dead and MTT assays are performed to evaluate the cell viability and proliferation of our prepared hydrogel based on the former research [66,67]. As it is obvious in Fig. 2(g), Group B demonstrates more cell viability, as there are no dead cells. Similarly, according to the MTT assay, Fig. 2(h), a significant difference (**** $P < 0.0001$) is observed between the cell viability and proliferation rate of Group A and Group B. While cell viability is declined in Group A strikingly (**** $P < 0.0001$) compared to the control group, which is a result of cell motif deficiency in alginate, cell proliferation in Group B is remarkably increased (**** $P < 0.0001$). The presence of HAM within Group B accounts for this higher viability and proliferation owing to the fact that HAM is rich in laminin, fibronectin, and various types of collagen, which acts as a basement membrane for HUVECs by providing RGD cell motifs [71–73].

3.5. Morphometric analysis of HUVECs by DHM

As stated in Section 2.10, the recorded holograms of the HUVECs are subjected to numerical reconstruction toward extraction of 3D information. Fig. 3 shows a representative reconstruction workflow from holograms of the HUVECs in the control group (2D cell culture plate). Figs. 3(a) and 3(b) are a recorded digital hologram and a magnified view of a region of interest indicated by yellowish rectangle. The interferometric fringes of appropriate density cross the cells and carry their phase information. From a single recorded hologram several arbitrary sized regions or the whole field of view can be chosen and subjected to reconstruction. Fig. 3(c) is the corresponding reference hologram which is taken to subtract the effect of unwanted contaminations and optical aberrations from the associated phase of the sample. In ASP both holograms are first Fourier transformed. The Fourier transform of the hologram is shown in Fig. 3(d), which includes three distinguished areas associated to the two twin images and the DC terms of Eq. (1)(1). The spatial frequencies of one of the images, indicated by a red rectangle, are selected and the rest ones are removed. Then the selected frequencies are FFT shifted to be positioned at the center of the Fourier space. The final spatial frequency pattern is subjected to numerical propagation to a demanded axial distance. In our experiments we usually record the holograms when the targeted cells are, as much as possible, in focus. Therefore, only a limited axial propagation is usually required. The propagation is applied in Fourier space and leads to the Fourier transform of the image complex amplitude, which by an inverse Fourier transform provides the complex amplitude of the holographic image. According to the Eqs. (2)(2) and (3)(3), the intensity image similar to what a conventional bright

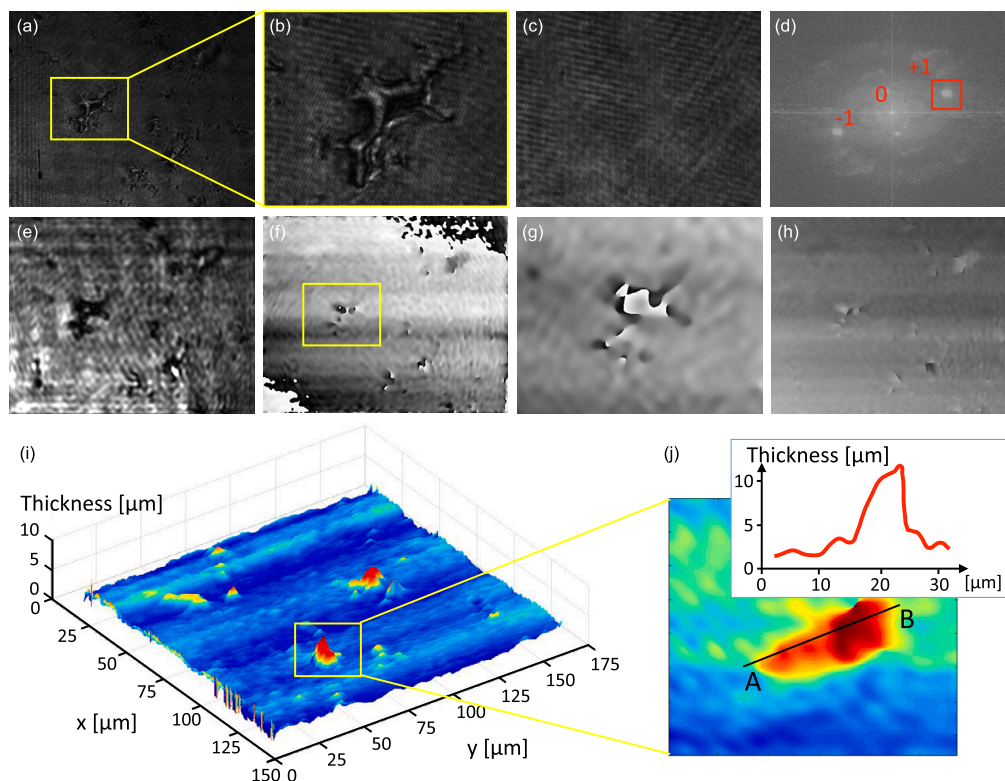


Fig. 3. A representative reconstruction workflow from holograms of the HUVECs in the control group (2D cell culture plate). (a) Recorded object digital hologram and (b) a magnified view of the selected region of interest. (c) Associated reference digital hologram. (d) Fourier spectrum of the hologram and selection of +1 order spatial frequencies. (e) Reconstructed intensity image. (f) Reconstructed filtered phase map after subtraction of the reference hologram's phase. (g) The smoothed phase map of the region of interest. (h) The unwrapped phase map. (i) 3D image, and (j) its 2D view with the cross-sectional thickness profile along the depicted AB line in the inset.

field microscopy provides, as well as the phase map of the samples are extracted from the reconstructed complex amplitude. Figs. 3(e) and 3(f) show the intensity image and the phase map after subtracting the effect of the reference hologram. A remarkable feature of DHM is that if needed additional filtering can also be applied in the reconstruction procedure. For example, for the acquired phase of Fig. 3(f), to minimize the so-called unwrapping errors (which will be explained in the following), we apply a 3×3 smoothing filter. However, it is also important that the filtering should not diminish the actual information of the sample. Fig. 3(g) is the filtered phase map of the region of interest in Fig. 3(a). Phase map throughout the xy plane and at each axial distance is obtained via a tangent function, which includes discontinuities at and similar points leading to a wrapped phase map. These discontinuities are removed by applying the unwrapping procedure. Several approaches have been introduced to obtain a continuous phase map. Amongst, we use the branch-cut algorithm which was first proposed by Goldstein [74]. The unwrapped phase map is shown in Fig. 3(h). Considering a negligible refractive index variations of the samples, the phase map provides the thickness of the sample at any (x, y) points, i.e. the 3D image (Eq. (3)). Figs. 3(i) and 3(j) are the reconstructed 3D image and its associated 2D map of the cell of Fig. 3(a), respectively. Given the thickness throughout the sample with a diffraction-limited resolution and an excellent axial precision is of high importance for several phase objects such as the ones in present research. This information leads eventually to a sufficiently high resolution quantitative phase image at an arbitrary time scale within the speed capabilities of the recording digital sensor.

In this research, the whole aforementioned procedure is performed on several HUVECs and the associated morphometrical parameters are calculated and discussed. The results suggest that HUVECs have a spindle-shaped morphology before being seeded on hydrogels.

3.6. Hydrogel characteristics optimization; 2D and 3D analyses

One of the underlying factors that directly influences the morphology of cells and their behavior is the surface characteristics, including roughness, pore size, and pore distribution, as though the pores should be small enough to let cell migration and large enough to let proliferation and secretion of new ECM and neovascularization [75,76]. Similarly, enhancement of the surface roughness of biomaterials, even at 10-100 nm scale, can increase the attachment and proliferation of HUVECs [71,72]. Here, we first take the advantage of FE-SEM images, and then the DHM results to demonstrate visually and quantitatively the difference in surface roughness and pore size before and after the addition of the powdered HAM to alginate. Figs. 4(a), 4(b), and 4(c) show the FE-SEM image of the surface and a cross-section of the alginate sample, and its DHM 3D morphometric image, respectively. Similar FE-SEM and DHM

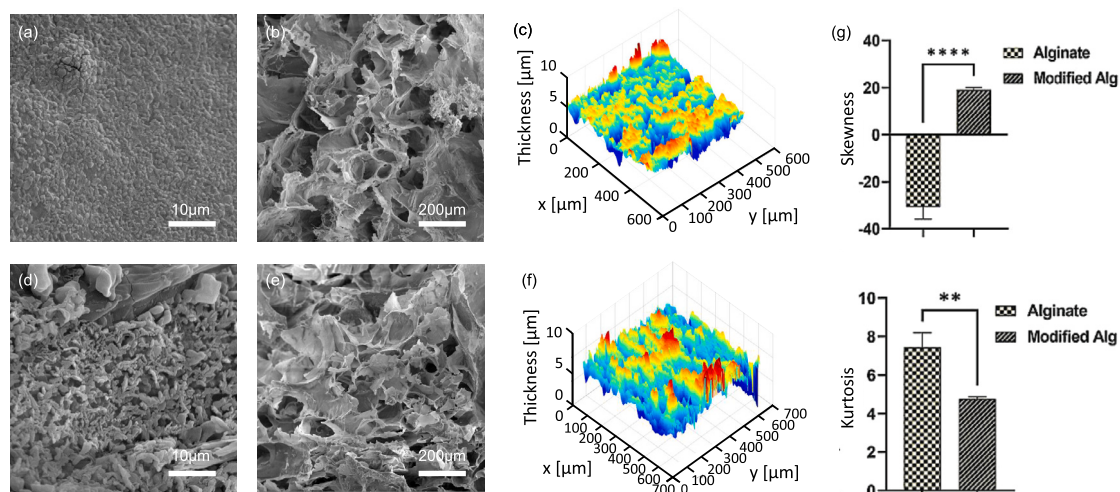


Fig. 4. FE-SEM and DHM images of alginate (a-c) and modified alginate (d-f). FE-SEM image of (a) the surface and (b) a cross-section of alginate sample, and (c) its DHM 3D morphometric image. (d), (e), (f) Similar FE-SEM and DHM images of alginate after adding powdered HAM. The images visually show the enhancement of porosity after modification. (g) The statistical roughness analysis of the DHM results for alginate and modified alginate cases.

images of alginate after adding powdered HAM are shown in Figs. 4(d), 4(e), and 4(f). It is visually evident that the surface roughness is increased in the modified alginate hydrogel group compared to the alginate hydrogel group due to the presence of powdered HAM. Analyzing the FE-SEM cross-sectional images provides the pore sizes. The results show that by adding the HAM powder the pore size decreases from $32.1 \pm 7.2 \mu\text{m}$ to $24.8 \pm 11 \mu\text{m}$. It is simply attributed to the occupation of the ambient parts of the pores by HAM particles which in turn results in a reduction of their sizes.

Considering the previous investigations, endothelial cells are adhesion-prone cells with an average size of 10-40 μm [77]. If the pores are larger than the HUVECs sizes (45-90 μm), the cell ceases to divide, and as a result, the proliferation diminishes. Consequently, the preferred pore size for HUVECs is in the range of their diameter (10-40 μm), which fits with our hydrogel pore size [77]. Moreover, our DHM analyses indicate that the roughness of the alginate hydrogel differs after being modified with HAM (Fig. 4(g)). The 3D DHM results show that the skewness of the alginate hydrogel modified with HAM is significantly higher than that of the alginate hydrogel (**** $p < 0.0001$), suggesting a skewness toward more positive values. This is obviously due to the occupation of the free spaces in hydrogel structures by HAM particles. Additionally, the kurtosis of the alginate hydrogel modified with HAM is significantly lower compared to the alginate hydrogel, probably due to the smaller pore sizes and pore walls (** $p = 0.0093$). This data suggests that the porous properties of the alginate hydrogel are improved after being modified with HAM. In the following steps, we performed a tube formation assay to check whether this improvement positively impacts the proliferation and migration of tube-forming endothelial cells.

3.7. Evaluation of endothelial tube formation

Angiogenesis, which comprises HUVECs viability, proliferation, migration, and tube formation, is of great significance in many physiological and pathological processes [78]. Taken together, angiogenesis is initiated by self-organizing HUVECs toward forming tube-like structures, which accounts for functional revascularization [5,79–81]. To evaluate the HUVECs tube formation, the live/dead assay is performed within 5 days and the results are concluded in Fig. 5. The 2D fluorescent images are analyzed using the “Angiogenesis Analyzer” (AA) plugin of ImageJ, which explains functional angiogenesis [1,5,79,82]. Herein, AA is applied to assess the meshing (tube) development and pseudo-capillary formation using the vectorial objects defined in Table 1. The 2D fluorescent images and their AA results for Group A are shown in Figs. 5(a) to 5(c). The associated DHM results for Group A which include volumetric information are shown in Fig. 5(d). Similarly, the 2D fluorescent images, AA analysis results, and the DHM reconstructed images for Group B are shown in Figs. 5(e), 5(f), 5(g), and 5(h), respectively. Obtained fluorescent images demonstrate excellent cell viability and angiogenesis within Group A and Group B. Seeding of HUVECs within a 3D bio-microenvironment of hydrogels instigates branching and the formation of an irregular mesh network. As demonstrated in Figs. 5(c) and 5(g), HUVECs spontaneously initiate the formation of Extremities, Segments, Branches, and self-alignment toward tube formation in Group A and Group B. The 3D reconstructed DHM images are in consistency with the fluorescent images. They demonstrate multiple imaging plane features at once, and avoids underestimation or overestimation of different morphological parameters. They indicate that, indeed, the tube formation and growth in both groups happen also in the axial direction, i.e., proving that the angiogenesis has a volumetric characteristic [40].

The above procedure is repeated and analyzed for several examinations. The aforementioned results are presented and compared in a more quantitative fashion in Figs. 5(i) to 5(m). According to Fig. 5(i), a significant difference is observed between Group A and Group B regarding the number of vectorial objects asserting more angiogenesis activity within Group B. By the same token, as meshes (tubes) formed by the alignment of adjacent segments, and since Group B possesses more meshes (tubes), a considerable difference is observed between the two groups in terms of total segments length (total tube length) as well as total mesh area (total tube area),

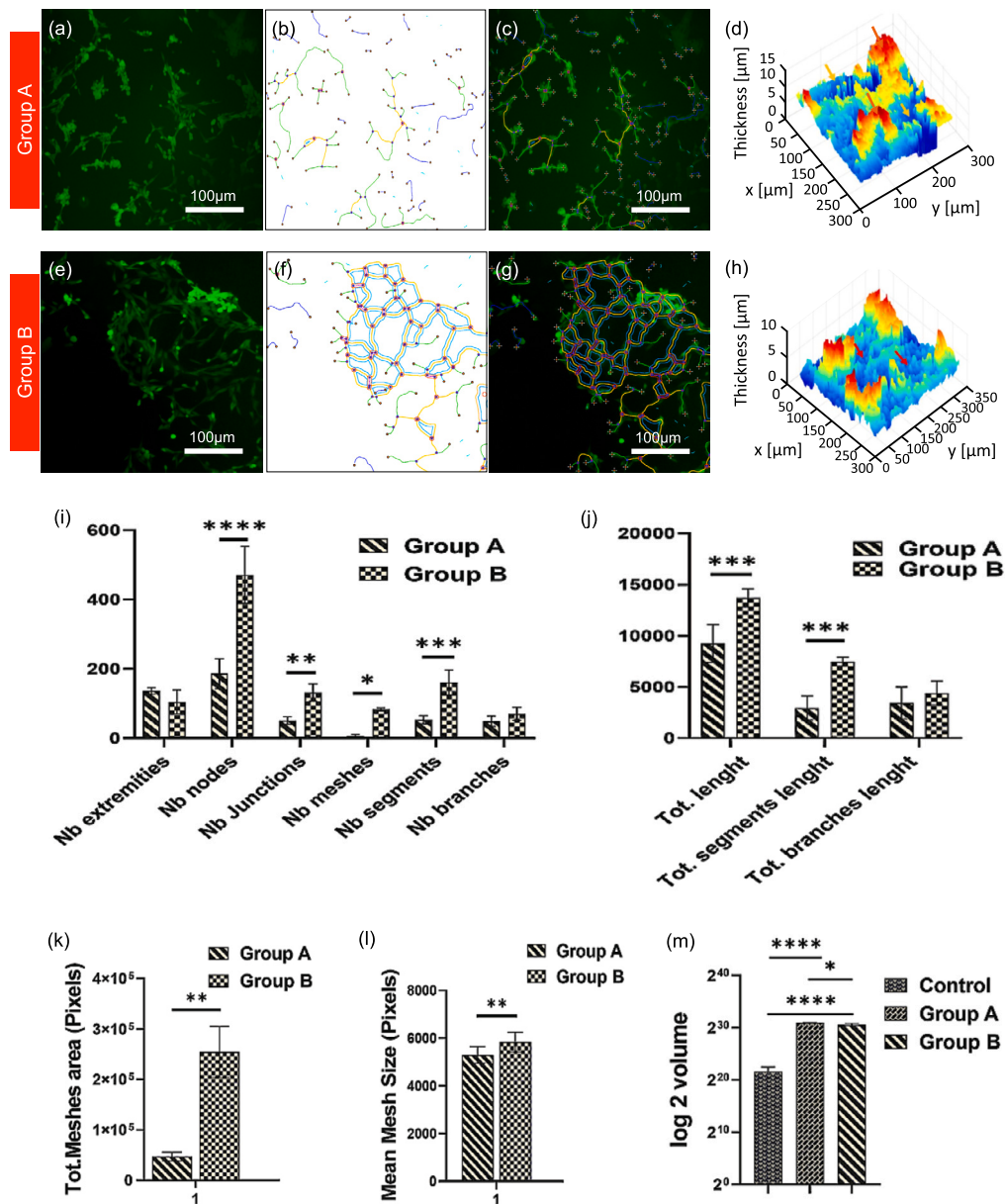


Fig. 5. 2D and 3D angiogenesis analyses. (a) Fluorescent images and their (b-c) ImageJ Angiogenesis Analyzer (AA) results for Group A; In panel (c) the analysis results and the image are overlaid for validation purposes; (d) The associated DHM reconstructed 3D image for Group A; (e-h) Similar fluorescent image, AA analysis, and DHM image for Group B; (i) Histogram of different vectorial objects in AA results for the two groups indicating more angiogenesis activity in the modified alginate (**** $P < 0.0001$, *** $P < 0.001$, ** $P < 0.005$, * $P < 0.01$); Similar comparison between the two groups in terms of (j) total segments length (total tube length), (k) total mesh area (total tube area), and (l) mean mesh size (average of tube length); (m) The cumulative node volume of HUVECs, obtained from DHM analysis for the two alginate hydrogel and modified alginate hydrogel groups (* $P < 0.01$, **** $P < 0.0001$). As depicted, adding the powder to the alginate hydrogel enhanced ECM support for HUVECs compared to the alginate hydrogel alone (orange arrows vs. red arrows).

as shown in Figs. 5(j) and 5(k), respectively. Similarly, the mean mesh size (average of tube length) augmented substantially in Group B (Fig. 5(l)). To evaluate the impact of modifying the alginate hydrogel with HAM, we compare the volume of every single endothelial cell with cells loaded in either alginate hydrogel or modified alginate hydrogel. Our data suggest that HAM reduces pore sizes and enhances HUVECs migration. However, in alginate hydrogel, HUVECs form nodes with tall and voluminous nodes with diminished migration due to large pore sizes compared to modified alginate. As depicted in Fig. 5(m), the cumulative node volume in the modified alginate group is therefore significantly lower than the alginate gel (* $p = 0.0321$). This evidence may suggest that modifying alginate hydrogel with HAM improves HUVECs migration by enhancing the pore sizes.

Altogether, encapsulated HUVECs within Group B demonstrate dramatic tube-formation (mesh development). Interestingly, besides the higher proliferation, HUVECs illustrated remarkable increases in Extremities, Segments, Branches, and Meshes (tubes)

number, confirming higher angiogenesis, which is owing to the presence of RGD units within Group B that provide sufficient cell motifs, confirming that mixing HAM within alginate provides an ECM-based membrane for HUVECs and noticeably enhances tube formation and angiogenic characteristics of the hydrogel [5,83–86].

We evaluated the influence of the 3D matrix on cellular behavior. The results obtained from viability, live-dead, and western blot assay demonstrated a significant difference between 2D cell culture in the plate and 3D cell encapsulation inside the alginate hydrogel and modified hydrogel, in terms of cell growth, elongation, and secretion of VEGF-R2 as the most significant activator of angiogenesis. The results showed that while alginate provides a 3D microenvironment for cells, which emulates the native tissue microenvironments, it demonstrated less proliferation compared with 2D cell culture [5]. The lack of cell attachment units in alginate accounts for this reduction bringing up that, whereas the 3D microenvironment is indispensable for cellular function, other key factors, such as cell-matrix interaction should also be considered. Similarly, alginate hydrogel expressed less VEGFR-2 compared with 2D culture [5], which again highlights the importance of cellular motifs for cell attachment, migration, and maturation. Modified alginate with decellularized HAM, nonetheless, demonstrated significant viability, elongation, and angiogenesis owing to providing essential cytokines, RGD cell attachment ligands, as well as the 3D microenvironment, revealing the importance of various biophysical parameters.

Combining decellularized HAM with alginate offers several benefits that enable it to closely replicate the microenvironment of natural tissues. While alginate hydrogel provides suitable mechanical stability and degradation rates [55,56], we have demonstrated that decellularized HAM enhances alginate's biocompatibility and promotes angiogenesis in ECs. We posit that this hydrogel holds significant promise for *in vitro* investigations. It offers a 3D biocompatible matrix that sustains extended cell proliferation, viability, and promotes angiogenesis. This feature set positions it as a potential platform for disease modeling and drug screening. The hydrogel scaffold shows potential as an ideal matrix in tissue engineering and regenerative medicine for developing mature vascular constructs, with its mechanical properties, such as elasticity, stiffness, and other biomechanical characteristics, being influenced by the ECM and varying based on its components, including proteoglycan, fibrin, elastin, and collagen. Moreover, given that the amniotic membrane has been successfully utilized in transplantation, such as cardiac patches, cornea, and skin, our scaffold can also be a strong candidate for further clinical investigations [25,26,87].

4. Conclusion

In conclusion the systematic experimental study presented in this paper provided two main results: (1) the different structures of the alginate hydrogel, i.e., being modified with human amniotic membrane, may impact the HUVECs tube formation capacity significantly, and (2) exploiting the 3D images provided by digital holographic microscopy, the method that we introduced in this study for quantitative label-free 3D imaging of angiogenesis, avoids underestimation or overestimation of morphological parameters of the process. It shows that the tube formation and growth happen also in the axial direction and proves that the angiogenesis has volumetric characteristics which are measured in terms of multiple morphometric parameters. The methodology presented here has the potential to be used for live imaging of further physiological procedures over time toward quantitative and volumetric monitoring and measurement of their dynamics.

CRedit authorship contribution statement

Faranak Heidari: Writing – review & editing, Writing – original draft, Visualization, Validation, Methodology, Investigation, Formal analysis, Data curation, Conceptualization, Resources. **Parisa Shamshiripour:** Methodology, Investigation, Visualization, Writing – review & editing. **Mehrana Rahnama:** Methodology, Investigation. **Maryam Saadatmand:** Writing – review & editing, Resources, Conceptualization, Formal analysis, Supervision. **Davoud Ahmadvand:** Methodology, Resources. **Sara Simorgh:** Writing – review & editing, Visualization, Supervision, Resources, Methodology, Investigation, Conceptualization, Project administration. **Ali-Reza Moradi:** Writing – review & editing, Visualization, Validation, Supervision, Software, Methodology, Investigation, Conceptualization, Project administration, Writing – original draft.

Declaration of competing interest

The authors declare that they have no known competing financial interests or personal relationships that could have appeared to influence the work reported in this paper.

Acknowledgement

We are grateful to the IUMS Core Facility Laboratory (ICL) for generously providing us with the essential tools and resources required to conduct our research.

Data availability

Data underlying the results presented in this paper are not publicly available at this time but may be obtained from the authors upon reasonable request.

References

- [1] J.-S. Lee, S. Chae, D. Yoon, D. Yoon, W. Chun, G.H. Kim, Angiogenic factors secreted from human ASC spheroids entrapped in an alginate-based hierarchical structure via combined 3D printing/electrospinning system, *Biofabrication* 12 (4) (2020) 045028.
- [2] T.J. Koob, J.J. Lim, M. Massee, N. Zabeck, R. Rennert, G. Gurtner, W.W. Li, Angiogenic properties of dehydrated human amnion/chorion allografts: therapeutic potential for soft tissue repair and regeneration, *Vasc. Cell* 6 (2014) 1–10.
- [3] G. Eelen, L. Treps, X. Li, P. Carmeliet, Basic and therapeutic aspects of angiogenesis updated, *Circ. Res.* 127 (2) (2020) 310–329.
- [4] S. Kargozar, F. Baino, S. Hamzehlou, M.R. Hamblin, M. Mozafari, Nanotechnology for angiogenesis: opportunities and challenges, *Chem. Soc. Rev.* 49 (14) (2020) 5008–5057.
- [5] F. Heidari, M. Saadatmand, S. Simorgh, Directly coaxial bioprinting of 3D vascularized tissue using novel bioink based on decellularized human amniotic membrane, *Int. J. Biol. Macromol.* 253 (2023) 127041.
- [6] G. Carpentier, S. Berndt, S. Ferratge, W. Rasband, M. Cuendet, G. Uzan, P. Albanese, Angiogenesis analyzer for imageJ—a comparative morphometric analysis of “endothelial tube formation assay” and “fibrin bead assay”, *Sci. Rep.* 10 (1) (2020) 11568.
- [7] E.A. Logsdon, S.D. Finley, A.S. Popel, F.M. Gabhann, A systems biology view of blood vessel growth and remodelling, *J. Cell. Mol. Med.* 18 (8) (2014) 1491–1508.
- [8] F.M. Ferguson, N.S. Gray, Kinase inhibitors: the road ahead, *Nat. Rev. Drug Discov.* 17 (5) (2018) 353–377.
- [9] S. Ferratge, G. Ha, G. Carpentier, N. Arouche, R. Bascetin, L. Muller, S. Germain, G. Uzan, Initial clonogenic potential of human endothelial progenitor cells is predictive of their further properties and establishes a functional hierarchy related to immaturity, *J. Stem Cell Res.* 21 (2017) 148–159.
- [10] A.V. Samarelli, E. Riccitelli, B. Bizzozero, T.N. Silveira, G. Seano, M. Pergolizzi, G. Vitagliano, I. Cascone, G. Carpentier, A. Bottos, et al., Neuroigin 1 induces blood vessel maturation by cooperating with the $\alpha 6$ integrin, *J. Biol. Chem.* 289 (28) (2014) 19466–19476.
- [11] J. Yu, Y. Gu, K.T. Du, S. Mihadja, R.E. Sievers, R.J. Lee, The effect of injected RGD modified alginate on angiogenesis and left ventricular function in a chronic rat infarct model, *Biomaterials* 30 (5) (2009) 751–756.
- [12] H.J. Lee, S. Mun, D.M. Pham, P. Kim, Extracellular matrix-based hydrogels to tailoring tumor organoids, *ACS Biomater. Sci. Eng.* 7 (9) (2021) 4128–4135.
- [13] K. Behan, A. Dufour, O. Garcia, D. Kelly, Methacrylated cartilage ECM-based hydrogels as injectables and bioinks for cartilage tissue engineering, *Biomolecules* 12 (2) (2022) 216.
- [14] Y. Luo, L. Fan, C. Liu, H. Wen, S. Wang, P. Guan, D. Chen, C. Ning, L. Zhou, G. Tan, An injectable, self-healing, electroconductive extracellular matrix-based hydrogel for enhancing tissue repair after traumatic spinal cord injury, *Bioact. Mater.* 7 (2022) 98–111.
- [15] Z. Bashiri, I. Amiri, M. Gholipourmalekabadi, R. Falak, H. Asgari, C.B. Maki, A. Moghaddaszadeh, M. Koruji, Artificial testis: a testicular tissue extracellular matrix as a potential bio-ink for 3D printing, *Biomater. Sci.* 9 (9) (2021) 3465–3484.
- [16] A. Azadbakht, S. Alizadeh, Z. Aliakbar Ahoven, Z. Khosrowpour, M. Majidi, S. Pakzad, S. Shojaei, N.P.S. Chauhan, M. Jafari, M. Gholipourmalekabadi, Chitosan-placental ECM composite thermos-responsive hydrogel as a biomimetic wound dressing with angiogenic property, *Macromol. Biosci.* 23 (2) (2023) 2200386.
- [17] Z. Bashiri, M.R. Fomeshi, H.G. Hamidabadi, D. Jafari, S. Alizadeh, M.N. Bojnordi, G. Orive, A. Dolatshahi-Pirouz, M. Zahiri, R.L. Reis, et al., 3D-printed placental-derived bioinks for skin tissue regeneration with improved angiogenesis and wound healing properties, *Mater. Today Bio* 20 (2023) 100666.
- [18] A. Kruger-Genge, S. Hauser, A.T. Neffe, Y. Liu, A. Lendlein, J. Pietzsch, F. Jung, Response of endothelial cells to gelatin-based hydrogels, *ACS Biomater. Sci. Eng.* 7 (2) (2021) 527–540.
- [19] T.T.A. Liguori, G.R. Liguori, J.A. van Dongen, L.F.P. Moreira, M.C. Harmsen, Bioactive decellularized cardiac extracellular matrix-based hydrogel as a sustained-release platform for human adipose tissue-derived stromal cell-secreted factors, *Biomed. Mater.* 16 (2) (2021) 025022.
- [20] G. Salimbeigi, N.E. Vrana, A.M. Ghaemmaghami, P.Y. Huri, G.B. McGuinness, Basement membrane properties and their recapitulation in organ-on-chip applications, *Mater. Today Bio* 15 (2022) 100301.
- [21] A.C. Hernández-González, L. Téllez-Jurado, L.M. Rodríguez-Lorenzo, Alginate hydrogels for bone tissue engineering, from injectables to bioprinting: a review, *Carbohydr. Polym.* 229 (2020) 115514.
- [22] M. Zhang, X. Zhao, Alginate hydrogel dressings for advanced wound management, *Int. J. Biol. Macromol.* 162 (2020) 1414–1428.
- [23] H. Nikniaz, Z. Zandieh, M. Nouri, N. Daei-Farshbaf, R. Aflatoonian, M. Gholipourmalekabadi, S.B. Jameie, Comparing various protocols of human and bovine ovarian tissue decellularization to prepare extracellular matrix-alginate scaffold for better follicle development in vitro, *BMC Biotechnol.* 21 (2021) 1–8.
- [24] M. Gholipourmalekabadi, N.P.S. Chauhan, B. Farhadhosseinabad, A. Samadikuchaksaraei, Human amniotic membrane as a biological source for regenerative medicine, in: *Perinatal Tissue-Derived Stem Cells: Alternative Sources of Fetal Stem Cells*, 2016, pp. 81–105.
- [25] A. Walkden, Amniotic membrane transplantation in ophthalmology: an updated perspective, *Clin. Ophthalmol.* (2020) 2057–2072.
- [26] G.G. Blume, P.A.B. Machado-Júnior, G.P. Bertinato, R.B. Simeoni, J.C. Francisco, L.C. Guarita-Souza, Tissue-engineered amniotic membrane in the treatment of myocardial infarction: a systematic review of experimental studies, *Am. J. Cardiovasc. Dis.* 11 (1) (2021) 1.
- [27] M.G.B. Pereira, J.A.P. Gomes, L.V. Rizzo, P.C. Cristovam, L.C. Silveira, Cytokine dosage in fresh and preserved human amniotic membrane, *Cornea* 35 (1) (2016) 89–94.
- [28] S. Leal-Marín, T. Kern, N. Hofmann, O. Pogozhykh, C. Framme, M. Börgel, C. Figueiredo, B. Glasmacher, O. Gryshkov, Human amniotic membrane: a review on tissue engineering, application, and storage, *J. Biomed. Mater. Res., Part B, Appl. Biomater.* 109 (8) (2021) 1198–1215.
- [29] Y.S. Kim, M. Majid, A.J. Melchiorri, A.G. Mikos, Applications of decellularized extracellular matrix in bone and cartilage tissue engineering, *Bioeng. Transl. Med.* 4 (1) (2019) 83–95.
- [30] M.K. Kim, W. Jeong, S.M. Lee, J.B. Kim, S. Jin, H.-W. Kang, Decellularized extracellular matrix-based bio-ink with enhanced 3D printability and mechanical properties, *Biofabrication* 12 (2) (2020) 025003.
- [31] A.J. Vernengo, S. Grad, D. Eglin, M. Alini, Z. Li, Bioprinting tissue analogues with decellularized extracellular matrix bioink for regeneration and tissue models of cartilage and intervertebral discs, *Adv. Funct. Mater.* 30 (44) (2020) 1909044.
- [32] M. Kesti, C. Eberhardt, G. Pagliccia, D. Kenkel, D. Grande, A. Boss, M. Zenobi-Wong, Bioprinting complex cartilaginous structures with clinically compliant biomaterials, *Adv. Funct. Mater.* 25 (48) (2015) 7406–7417.
- [33] M. Becker, J.A. Maring, M. Schneider, A.X. Herrera Martin, M. Seifert, O. Klein, T. Braun, V. Falk, C. Stamm, Towards a novel patch material for cardiac applications: tissue-specific extracellular matrix introduces essential key features to decellularized amniotic membrane, *Int. J. Mol. Sci.* 19 (4) (2018) 1032.
- [34] A. Cagnoni, M. Di Marcello, M. Campagnol, C. Nassuato, A. Albertini, O. Parolini, Amniotic membrane patching promotes ischemic rat heart repair, *Cell Transplant* 18 (10–11) (2009) 1147–1159.
- [35] I. Arnaoutova, J. George, H.K. Kleinman, G. Benton, The endothelial cell tube formation assay on basement membrane turns 20: state of the science and the art, *Angiogenesis* 12 (2009) 267–274.
- [36] I. Arnaoutova, H.K. Kleinman, In vitro angiogenesis: endothelial cell tube formation on gelled basement membrane extract, *Nat. Protoc.* 5 (4) (2010) 628–635.
- [37] Z.I. Stryker, M. Rajabi, P.J. Davis, S.A. Mousa, Evaluation of angiogenesis assays, *Biomedicine* 7 (2) (2019) 37.
- [38] R.M. Brown, C.J. Meah, V.L. Heath, I.B. Styles, R. Bicknell, Tube-forming assays, in: *Angiogenesis Protocols*, 2016, pp. 149–157.
- [39] M.N. Nakatsu, C.C. Hughes, Chapter 4 an optimized three dimensional in vitro model for the analysis of angiogenesis, in: *Methods in Enzymology*, vol. 443, Academic Press, 2008, pp. 65–82, <https://www.sciencedirect.com/science/article/pii/S0076687908020041>.
- [40] J. Gu, R. Ternifi, S. Sabeti, N.B. Larson, J.M. Carter, R.T. Fazio, M. Fatemi, A. Alizad, Volumetric imaging and morphometric analysis of breast tumor angiogenesis using a new contrast-free ultrasound technique: a feasibility study, *Breast Cancer Res.* 24 (1) (2022) 85.
- [41] J.W. Lichtman, J.-A. Conchello, Fluorescence microscopy, *Nat. Methods* 2 (12) (2005) 910–919.

- [42] N. Fathi, A.-R. Moradi, M. Habibi, D. Vashae, L. Tayebi, Digital holographic microscopy of the myelin figure structural dynamics and the effect of thermal gradient, *Biomed. Opt. Express* 4 (6) (2013) 950–957.
- [43] Y.-S. Choi, S.-J. Lee, Three-dimensional volumetric measurement of red blood cell motion using digital holographic microscopy, *Appl. Opt.* 48 (16) (2009) 2983–2990.
- [44] E. Shaffer, C. Moratal, P. Magistretti, P. Marquet, C. Depeursinge, Label-free second-harmonic phase imaging of biological specimen by digital holographic microscopy, *Opt. Lett.* 35 (24) (2010) 4102–4104.
- [45] K.W. Seo, E. Seo, S.J. Lee, Cellular imaging using phase holographic microscopy: for the study of pathophysiology of red blood cells and human umbilical vein endothelial cells, *J. Vis.* 17 (2014) 235–244.
- [46] K. Lee, K. Kim, J. Jung, J. Heo, S. Cho, S. Lee, G. Chang, Y. Jo, H. Park, Y. Park, Quantitative phase imaging techniques for the study of cell pathophysiology: from principles to applications, *Sensors* 13 (4) (2013) 4170–4191.
- [47] T. Tahara, X. Quan, R. Otani, Y. Takaki, O. Matoba, Digital holography and its multidimensional imaging applications: a review, *Microscopy* 67 (2) (2018) 55–67.
- [48] R. Mosaviani, A.-R. Moradi, L. Tayebi, Effect of humidity on liquid-crystalline myelin figure growth using digital holographic microscopy, *Mater. Lett.* 173 (2016) 162–166.
- [49] M.A. Panahi, Z. Tahmasebi, V. Abbasian, M. Amiri, A.-R. Moradi, Role of pH level on the morphology and growth rate of myelin figures, *Biomed. Opt. Express* 11 (10) (2020) 5565–5574.
- [50] V.F. Rad, A. Babaee-Ghazvini, R. Jamali, I. Shahabi-Ghahfarrokhi, A.-R. Moradi, Digital holographic microscopy for real-time investigation of 3D microstructural dynamics of starch-kefir-based nanocomposite, *Appl. Opt.* 60 (16) (2021) 4706–4715.
- [51] M. Panahi, R. Jamali, V.F. Rad, M. Khorasani, A. Darudi, A.-R. Moradi, 3d monitoring of the surface slippage effect on micro-particle sedimentation by digital holographic microscopy, *Sci. Rep.* 11 (1) (2021) 12916.
- [52] S. Khosravimelal, M. Momeni, M. Gholipur, S.C. Kundu, M. Gholipourmalekabadi, Protocols for Decellularization of Human Amniotic Membrane, *Methods in Cell Biology*, vol. 157, Elsevier, 2020, pp. 37–47.
- [53] M. Gholipourmalekabadi, B. Farhadhosseiniabadi, M. Faraji, M.R. Nourani, How preparation and preservation procedures affect the properties of amniotic membrane? How safe are the procedures?, *Burns* 46 (6) (2020) 1254–1271.
- [54] A. Mousavi, S. Mashayekhan, N. Baheiraei, A. Pourjavadi, Biohybrid oxidized alginate/myocardial extracellular matrix injectable hydrogels with improved electromechanical properties for cardiac tissue engineering, *Int. J. Biol. Macromol.* 180 (2021) 692–708.
- [55] W. Liu, H. Madry, M. Cucchiari, Application of alginate hydrogels for next-generation articular cartilage regeneration, *Int. J. Mol. Sci.* 23 (3) (2022) 1147.
- [56] D. Ji, J.M. Park, M.S. Oh, T.L. Nguyen, H. Shin, J.S. Kim, D. Kim, H.S. Park, J. Kim, Superstrong, superstiff, and conductive alginate hydrogels, *Nat. Commun.* 13 (1) (2022) 3019.
- [57] M.I. Neves, L. Moroni, C.C. Barrias, Modulating alginate hydrogels for improved biological performance as cellular 3D microenvironments, *Front. Bioeng. Biotechnol.* 8 (2020) 665.
- [58] S. Khalighi, M. Saadatmand, Bioprinting a thick and cell-laden partially oxidized alginate-gelatin scaffold with embedded micro-channels as future soft tissue platform, *Int. J. Biol. Macromol.* 193 (2021) 2153–2164.
- [59] M. Firoozi, M. Entezam, E. Masaeli, F. Ejeian, M.H. Nasr-Esfahani, Physical modification approaches to enhance cell supporting potential of poly (vinyl alcohol)-based hydrogels, *J. Appl. Polym. Sci.* 139 (2) (2022) 51485.
- [60] S. Kamiloglu Bestepe, G. Sari, T. Özdal, E. Çapanoğlu Güven, Guidelines for cell viability assays, *Food Front.* 1 (3) (2020).
- [61] S. Simorgh, P.B. Milan, M. Saadatmand, Z. Bagher, M. Gholipourmalekabadi, R. Alizadeh, A. Hivechi, Z. Arabpour, M. Hamidi, C. Delattre, Human olfactory mucosa stem cells delivery using a collagen hydrogel: as a potential candidate for bone tissue engineering, *Materials* 14 (14) (2021) 3909.
- [62] P. Zare, M. Pezeshki-Modaress, S.M. Davachi, H. Chahsetareh, S. Simorgh, N. Asgari, M.A. Haramshahi, R. Alizadeh, Z. Bagher, M. Farhadi, An additive manufacturing-based 3D printed poly ϵ -caprolactone/alginate sulfate/extracellular matrix construct for nasal cartilage regeneration, *J. Biomed. Mater. Res., Part A* 110 (6) (2022) 1199–1209.
- [63] V. Farzam Rad, R. Tavakkoli, A.-R. Moradi, A. Anand, B. Javidi, Calcium effect on membrane of an optically trapped erythrocyte studied by digital holographic microscopy, *Appl. Phys. Lett.* 111 (8) (2017).
- [64] M. Tamimi, S. Rajabi, M. Pezeshki-Modaress, Cardiac ECM/chitosan/alginate ternary scaffolds for cardiac tissue engineering application, *Int. J. Biol. Macromol.* 164 (2020) 389–402.
- [65] R. Najafi, H. Chahsetareh, M. Pezeshki-Modaress, M. Aleemardani, S. Simorgh, S.M. Davachi, R. Alizadeh, A. Asghari, S. Hassanzadeh, Z. Bagher, Alginate sulfate/ECM composite hydrogel containing electrospun nanofiber with encapsulated human adipose-derived stem cells for cartilage tissue engineering, *Int. J. Biol. Macromol.* 238 (2023) 124098.
- [66] S.K. Papageorgiou, E.P. Kouvelos, E.P. Favvas, A.A. Sapolidis, G.E. Romanos, F.K. Katsaros, Metal–carboxylate interactions in metal–alginate complexes studied with FTIR spectroscopy, *Carbohydr. Res.* 345 (4) (2010) 469–473.
- [67] S.R. Derkach, N.G. Voron'ko, N.I. Sokolan, D.S. Kolotova, Y.A. Kuchina, Interactions between gelatin and sodium alginate: UV and FTIR studies, *J. Dispers. Sci. Technol.* (2019).
- [68] A. Saarai, V. Kasparkova, T. Sedlacek, P. Saha, On the development and characterisation of crosslinked sodium alginate/gelatin hydrogels, *J. Mech. Behav. Biomed. Mater.* 18 (2013) 152–166.
- [69] A.C. Villamil Ballesteros, H.R. Segura Puello, J.A. Lopez-Garcia, A. Bernal-Ballen, D.L. Nieto Mosquera, D.M. Munoz Forero, J.S. Segura Charry, Y.A. Neira Bejarano, Bovine decellularized amniotic membrane: extracellular matrix as scaffold for mammalian skin, *Polymers* 12 (3) (2020) 590.
- [70] L.I.S. Naasani, A.F.D. Souza, C. Rodrigues, S. Vedovatto, J.G. Azevedo, A.P.S. Bertoni, M.D.C. Fernandes, S. Buchner, M.R. Wink, Decellularized human amniotic membrane associated with adipose derived mesenchymal stromal cells as a bioscaffold: physical, histological and molecular analysis, *Biochem. Eng. J.* 152 (2019) 107366.
- [71] P.-H. Lee, S.-H. Tsai, L. Kuo, C.-Y. Hwang, C.-Y. Kuo, V.C. Yang, J.-K. Chen, A prototype tissue engineered blood vessel using amniotic membrane as scaffold, *Acta Biomater.* 8 (9) (2012) 3342–3348.
- [72] S.-H. Tsai, Y.-W. Liu, W.-C. Tang, Z.-W. Zhou, C.-Y. Hwang, G.-Y. Hwang, B.-R. Ou, C.-P. Hu, V.C. Yang, J.-K. Chen, Characterization of porcine arterial endothelial cells cultured on amniotic membrane, a potential matrix for vascular tissue engineering, *Biochem. Biophys. Res. Commun.* 357 (4) (2007) 984–990.
- [73] S. Aslani, M. Kabiri, M. Kehtari, H. Hanaee-Ahvaz, Vascular tissue engineering: fabrication and characterization of acetylsalicylic acid-loaded electrospun scaffolds coated with amniotic membrane lysate, *J. Cell. Physiol.* 234 (9) (2019) 16080–16096.
- [74] B. Gutmann, H. Weber, Phase unwrapping with the branch-cut method: role of phase-field direction, *Appl. Opt.* 39 (26) (2000) 4802–4816.
- [75] A. Hivechi, S.H. Bahrami, R.A. Siegel, A. Siehr, A. Sahoo, P.B. Milan, M.T. Joghataei, M. Amoupour, S. Simorgh, Cellulose nanocrystal effect on crystallization kinetics and biological properties of electrospun polycaprolactone, *Mater. Sci. Eng., C* 121 (2021) 111855.
- [76] S. Simorgh, Z. Bagher, M. Farhadi, S.K. Kamrava, M.E. Boroujeni, Z. Namjoo, F.Q. Hour, S. Moradi, R. Alizadeh, Magnetic targeting of human olfactory mucosa stem cells following intranasal administration: a novel approach to Parkinson's disease treatment, *Mol. Neurobiol.* 58 (2021) 3835–3847.
- [77] D. Narayan, S. Venkatraman, Effect of pore size and interpore distance on endothelial cell growth on polymers, *J. Biomed. Mater. Res., Part A* 87 (3) (2008) 710–718.
- [78] X. Wang, A.M. Bove, G. Simone, B. Ma, Molecular bases of vegfr-2-mediated physiological function and pathological role, *Front. Cell Dev. Biol.* 8 (2020) 599281.
- [79] S. Nemati, A. Rezabakhsh, A.B. Khoshfetrat, A. Nourazarian, Ç. Biray Avcı, B. Goker Bagca, H. Alizadeh Sardroud, M. Khaksar, M. Ahmadi, A. Delkosh, et al., Alginate-gelatin encapsulation of human endothelial cells promoted angiogenesis in vivo and in vitro milieu, *Biotechnol. Bioeng.* 114 (12) (2017) 2920–2930.

- [80] M.A. Redd, N. Zeinstra, W. Qin, W. Wei, A. Martinson, Y. Wang, R.K. Wang, C.E. Murry, Y. Zheng, Patterned human microvascular grafts enable rapid vascularization and increase perfusion in infarcted rat hearts, *Nat. Commun.* 10 (1) (2019) 584.
- [81] C. Piard, H. Baker, T. Kamalidinov, J. Fisher, Bioprinted osteon-like scaffolds enhance in vivo neovascularization, *Biofabrication* 11 (2) (2019) 025013.
- [82] J. Ao, T. Chiba, S. Shibata, A. Kurosugi, N. Qiang, Y. Ma, M. Kan, T. Iwanaga, T. Sakuma, H. Kanzaki, et al., Acquisition of mesenchymal-like phenotypes and overproduction of angiogenic factors in lenvatinib-resistant hepatocellular carcinoma cells, *Biochem. Biophys. Res. Commun.* 549 (2021) 171–178.
- [83] Y.H. Song, S.H. Shon, M. Shan, A.D. Stroock, C. Fischbach, Adipose-derived stem cells increase angiogenesis through matrix metalloproteinase-dependent collagen remodeling, *Integr. Biol.* 8 (2) (2016) 205–215.
- [84] M. Zoughaib, D. Luong, R. Garifullin, D.Z. Gatina, S.V. Fedosimova, T.I. Abdullin, Enhanced angiogenic effects of RGD, GHK peptides and copper (ii) compositions in synthetic cryogel ECM model, *Mater. Sci. Eng., C* 120 (2021) 111660.
- [85] A. Faiz, L.M. Harkness, G. Tjin, V. Bernal, P. Horvatovich, A. James, J.G. Elliot, J.K. Burgess, A.W. Ashton, Angiogenic regulatory influence of extracellular matrix deposited by resting state asthmatic and non-asthmatic airway smooth muscle cells is similar, *J. Cell. Mol. Med.* 25 (13) (2021) 6438–6447.
- [86] C. Fedele, M. De Gregorio, P.A. Netti, S. Cavalli, C. Attanasio, Azopolymer photopatterning for directional control of angiogenesis, *Acta Biomater.* 63 (2017) 317–325.
- [87] Y. Yang, Y. Zhang, Y. Yan, Q. Ji, Y. Dai, S. Jin, Y. Liu, J. Chen, L. Teng, A sponge-like double-layer wound dressing with chitosan and decellularized bovine amniotic membrane for promoting diabetic wound healing, *Polymers* 12 (3) (2020) 535.